Modeling of a Scan Type Magnetic Camera Image Using the Improved Dipole Model

Jiseong Hwang
Graduate School, Chosun University,
375 Seosuk-dong, Dong-gu, Gwangju 501-759, Korea
Jinyi Lee*
Department of Control and Instrument Engineering, Chosun University,
375 Seosuk-dong, Dong-gu, Gwangju 501-759, Korea

The scan type magnetic camera is proposed to improve the limited spatial resolution due to the size of the packaged magnetic sensor. An image of the scan type magnetic camera, $\partial B/\partial x$ image, is useful for extracting the crack information of a specimen under a large inclined magnetic field distribution due to the poles of magnetizer. The $\partial B/\partial x$ images of the cracks of different shapes and sizes are calculated by using the improved dipole model proposed in this paper. The improved dipole model uses small divided dipole models, the rotation and relocation of each dipole model and the principle of superposition. Also for a low carbon steel specimen, the experimental results of nondestructive testing obtained by using multiple cracks are compared with the modeling results to verify the effectiveness of $\partial B/\partial x$ modeling. The improved dipole model can be used to simulate the LMF and $\partial B/\partial x$ image of a specimen with complex cracks, and to evaluate the cracks quantitatively using magnetic flux leakage testing.

Key Words : Nondestructive Evaluation, Scan Type Magnetic Camera, Leakage Magnetic Flux, Dipole Model, Quantitative Modeling, Multiple Cracks

Nomenclature

B : Magnetic flux leakage [mT]
d : Depth [mm]
l : Length [mm]
m : Magnetic charge per unit area [mT]
u : Depth from specimen surface [mm]
w : Width [mm]
X : Magnetization direction
x : X-directional position
XY : Plane of the specimen surface
Y : Vertical direction to the X-axis on the XY plane
y : Y-directional position
Z : Vertical direction to the specimen surface
z : Z-directional position

Greek letters

Δx : Scanning interval of the scan type magnetic camera [mm]
μ : Magnetic permeability [mT/mT]
θ : Rotation angle of crack [degree]
$\partial B/\partial x$: Differential leakage magnetic flux to the x-directional distance [mT/mm]

Subscripts

C : Crack
offset : Offset from the center of the specimen
R : Rotated axis and position
Z : Vertical component

* Corresponding Author,
E-mail : jinyilee@chosun.ac.kr
TEL : +82-62-230-1701; **FAX** : +82-62-230-6858
Department of Control and Instrument Engineering, Chosun University, 375 Seosuk-dong, Dong-gu, Gwangju 501-759, Korea. (Manuscript **Received** March 3, 2006; **Revised** June 26, 2006)

1. Introduction

Large structures such as nuclear power, thermal power, chemical and petroleum refining plants

are drawing interest from the economic aspect of extending design life. However, poor environment, such as high pressure, high temperature, fatigue and corrosion, reduces their designed life spans. For extending design life, the degradation of and defects in aged structures must be evaluated. Among the different methods available for this task, nondestructive testing using the magnetic method is effective. It can predict and evaluate cracks on the surface of ferromagnetic structures.

In magnetic particle testing, magnetic particles are collected as the similar shape of crack due to leakage magnetic flux (hereafter LMF) around the crack. Therefore, when the ferromagnetic specimen is magnetized and magnetic particles are sprinkled, the cracks can be observed. However, to observe this crack, the specimen must be cleaned. Moreover, cracks and similar defects are difficult to distinguish from one another, so quantitative evaluation is difficult. On the other hand, magnetic flux leakage testing (hereafter MFLT) uses a magnetic sensor to detect the LMF distribution around a crack of a magnetized specimen. MFLT is used mainly to test for small defects in a thin steel plate of thickness less than 0.6 mm. MFLT can be used for quantitative nondestructive evaluation of a material. However, the magnetic sensor must be located close to the specimen surface (Yamada et al., 2001) because the LMF of a defect is spatially small and has weak intensity. This technique is also time-consuming because it uses a single sensor for measurement and analysis. On the other hand, magneto-optical nondestructive testing (Lee et al., 1998a ; 1998b ; 2000 ; 2004 ; 2005) is a kind of MFLT. The vertical component of LMF, is developed by the crack in a specimen, magnetizes the magnetic domain of the magneto-optical film. And the shape of this magnetic domain can be observed by the Faraday's effect, which is also used to detect cracks. However, this method in MFLT is also limited because the sensor has to be placed close to the specimen surface.

On the other hand, the lift-off needs to be increased to detect cracks under poor environment, such as high pressure, high temperature, vibration and dust. Therefore, a new technique of increasing and concentrating LMF is strongly demanded. The proposed magnetic camera (Lee et al., 2004a ; 2004b ; 2004c ; 2006a ; 2006b ; 2006c ; 2006d) is an apparatus that can quantitatively visualize the distribution of LMF around cracks on a magnetized specimen. Weak LMF can be concentrated onto the magnetic lens (Lee et al., 2004c ; 2006b ; 2006d), which is on the opposite side of the arrayed magnetic sensors, and the weak electrical signals from the sensor array can be amplified. The scan type magnetic camera (Lee et al., 2006a ; 2006c ; 2006d), especially, was proposed to overcome spatial limitation due to sensor size, and to obtain a high spatial resolution of LMF distribution. If a specimen flows under the sensors at a constant velocity, such as in the continuous casting processing, and the sensors are inclined in the direction of flow, high spatial resolution can be obtained. An image of the scan type magnetic camera, $\partial B/\partial x$ image, which shows the distribution of the differential LMF to the magnetization directional distance, is useful for extracting crack information (Lee et al., 2006a) from a specimen under a large inclined magnetic field distribution which is caused by the poles of the magnetizer.

This study proposes the quantitative numerical modeling of the $\partial B/\partial x$ images of the scan type magnetic camera by use of an improved dipole model. Also, for the low carbon steel specimen, the results obtained from testing that considered cracks of different sizes and shapes are compared with the modeling results to verify the effectiveness of $\partial B/\partial x$ image modeling.

2. Basic Principle

2.1 Scan type magnetic camera

As shown in Fig. 1, the magnetic camera is composed of the magnetic source, object, magnetic sensor array, magnetic lens, analog-to-digital converter, computer and monitor. Using these constructions, the distorted magnetic field around an object or the LMF around a crack is amplified and obtained.

To detect and evaluate the cracks on a fer-

romagnetic specimen, the specimen is magnetized by using a yoke type magnetizer, as shown in Fig. 2(a). Also, the sensor head, as shown in Fig. 2 (b), is fixed at the motorized xyz stage, as shown in Fig. 2(a), and scanned on the specimen surface with homogeneous lift-off. Furthermore, the inclined sensors in the direction of scanning are arrayed, as shown in Fig. 2(c), at the bottom of the sensor head to obtain high spatial resolution from a limited-size packaged senor in the scan type magnetic camera. The magnetic lens can be positioned at the back of the sensor array, as shown in Fig. 2(b), but is not introduced in this paper.

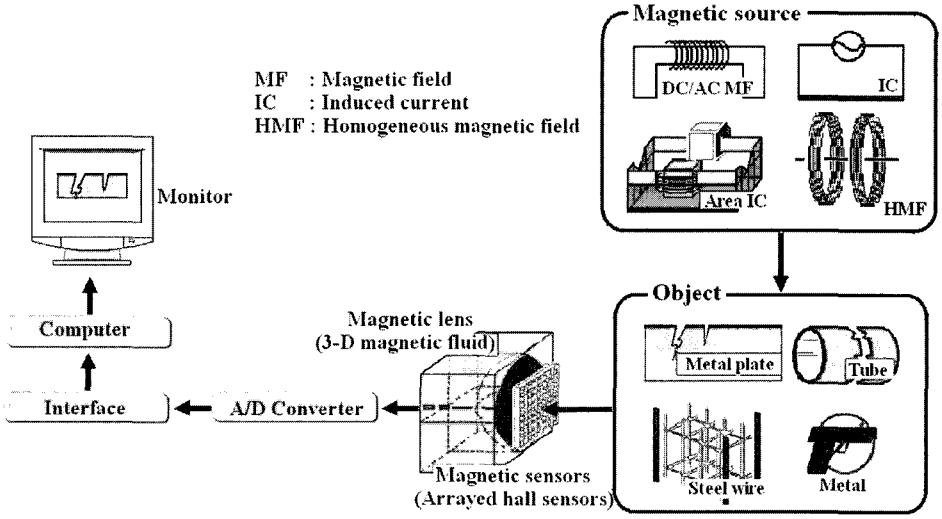

Fig. 1 Schematic of the magnetic camera

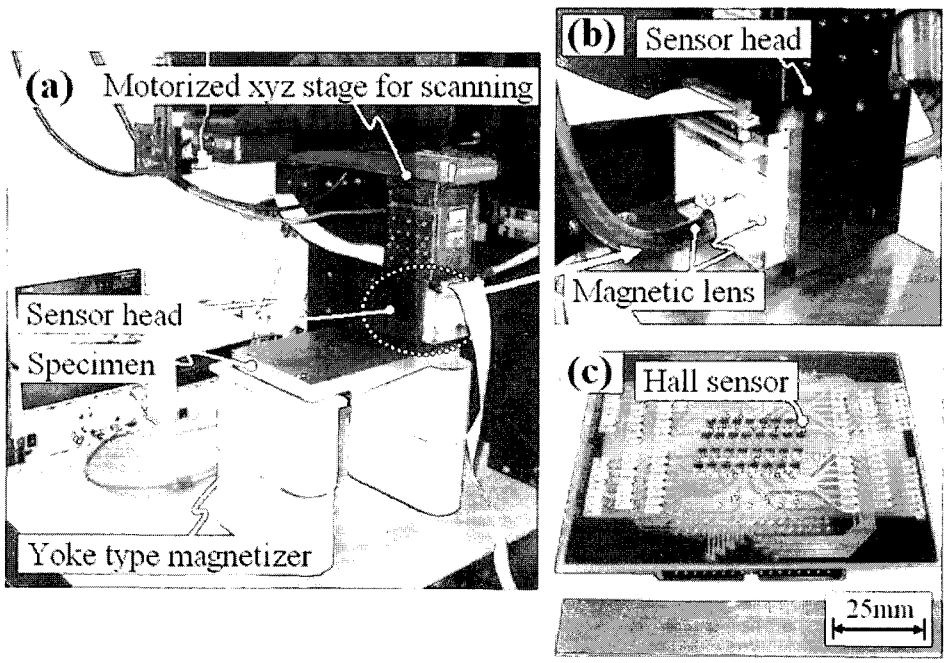

Fig. 2 Scan type magnetic camera

2.2 Improved dipole model and modeling of $\partial B/\partial x$ image

A crack of length of lc, width of wc, and depth of dc was introduced on the specimen surface. The X-axis was defined as the direction of magnetization; XY-plane, as the specimen surface; and Z-axis, as the vertical direction to the specimen surface, as shown in Fig. 3. Suppose that the crack is rotated θ_c from the Y-axis, as shown in Fig. 3. The direction of the crack length is in parallel with the Y-axis when $\theta_c=0$.

The Z-direction component of the LMF at the (x, y, z) position, B_z, can be expressed by the Eq. (1) using the dipole model (Minkov et al., 2000; Mukae et al., 1988; Lee et al., 2000; 2004; 2005) when $\theta_c=0$, where m, μ and u are the magnetic charge per unit area, magnetic permeability, and the depth from the specimen surface, respectively. The u has a value between $0\sim d_c$.

$$B_z|_{\theta_c=0}=\frac{m}{4\pi\mu}\int_{-l_c/2-y}^{l_c/2-y}\int_0^{d_c}\frac{z+u}{\{(x+w_c/2)^2+y^2+(z+u)^2\}^{3/2}}dudy - \frac{m}{4\pi\mu}\int_{-l_c/2-y}^{l_c/2-y}\int_0^{d_c}\frac{z+u}{\{(x-w_c/2)^2+y^2+(z+u)^2\}^{3/2}}dudy \quad (1)$$

On the other hand, x_R and y_R, which are the new locations on the rotated coordinate system X_R-Y_R axis at the rotate angle of θ_c from XY plane, as shown in Fig. 3, can be shown with Eq. (2).

$$x_R=\sqrt{x^2+y^2}\cos\left[\theta_c+\tan^{-1}\left(\frac{y}{x}\right)\right]$$
$$y_R=\sqrt{x^2+y^2}\sin\left[\theta_c+\tan^{-1}\left(\frac{y}{x}\right)\right] \quad (2)$$

In the case of $\theta_c=\pi/2$, B_Z according to Eq. (1) can be calculated by replacing w_C and l_C. Also, B_Z can be calculated with Eq. (3) (Lee et al., 2004) in the case of $0<\theta_c<\pi/2$.

$$B_z|_{0<\theta_c=0}=\frac{m\cos\theta_c}{4\pi\mu}\int_{-l_c/2-y_R}^{l_c/2-y_R}\int_0^{l_c}\frac{z+u}{\{(x_R+w_c/2)^2+y_R^2+(z+u)^2\}^{3/2}}dudy_R - \frac{m\cos\theta_c}{4\pi\mu}\int_{-l_c/2-y_R}^{l_c/2-y_R}\int_0^{l_c}\frac{z+u}{\{(x_R-w_c/2)^2+y_R^2+(z+u)^2\}^{3/2}}dudy_R \quad (3)$$

Furthermore, when the crack is located x_{offset}, y_{offset} from the center of the specimen as shown in Fig. 4, the x_R and y_R can be expressed as Eq. (4) by substituting Eq. (2). Fig. 4 shows the improvement of the dipole model when the crack is relocated from the center of specimen.

$$x_R=\sqrt{(x-x_{offset})^2+(y-y_{offset})^2}\cos\left[\theta_c+\tan^{-1}\left(\frac{y-y_{offset}}{x-x_{offset}}\right)\right]$$
$$y_R=\sqrt{(x-x_{offset})^2+(y-y_{offset})^2}\sin\left[\theta_c+\tan^{-1}\left(\frac{y-y_{offset}}{x-x_{offset}}\right)\right] \quad (4)$$

Also, a complex-shaped crack, such as a ring-shaped crack, as shown in Fig. 5, can be considered as a distribution of small cracks, which can be expressed by using Eqs. (1) ~ (4) and can

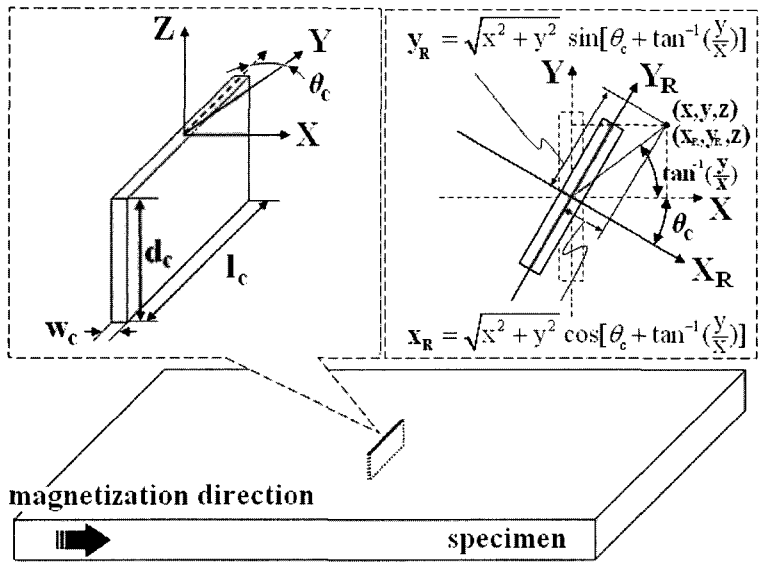

Fig. 3 Dipole model of crack

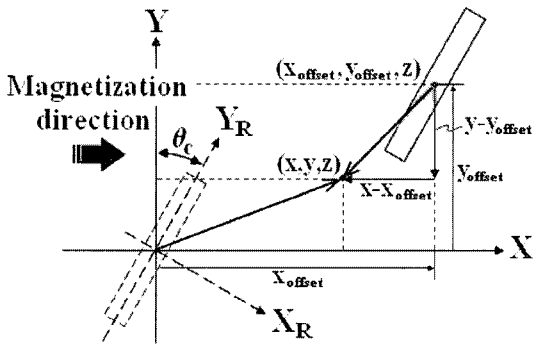

Fig. 4 Improvement of the dipole model when the crack is relocated from the center of specimen

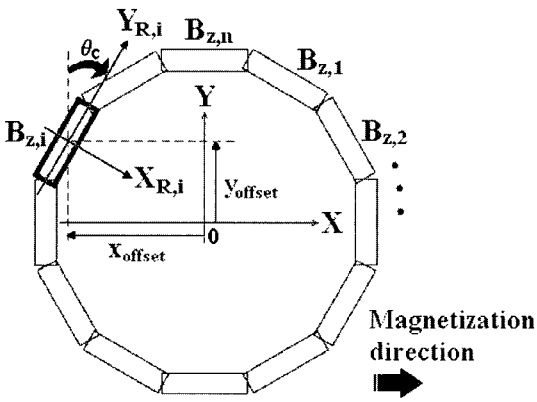

Fig. 5 Expression of the complex crack using the dipole model

be expressed by Eq. (5) using the principle of superposition.

$$B_{z,total}=\sum_{i=1}^{n}B_{z,i} \tag{5}$$

Conversely, $\partial B/\partial x$ processing means the differential LMF to the X-directional distance. Correspondingly, the $\partial B/\partial x$ image can be simplified by using Eq. (6). The Δx is 0.5 mm, which is the scanning interval of the scan type magnetic camera in this paper.

$$\frac{\partial B}{\partial x}(x,y,z)\approx\frac{B_{z,total}(x+\Delta x,y,z)-B_{z,total}(x,y,z)}{\Delta x} \tag{6}$$

3. Numerical Analysis and Experimental Results

Carbon steel specimen was prepared to a size of 160×135×20 mm, and its surface was mechanically polished. Multiple cracks of several different shapes and sizes were introduced on the speci-

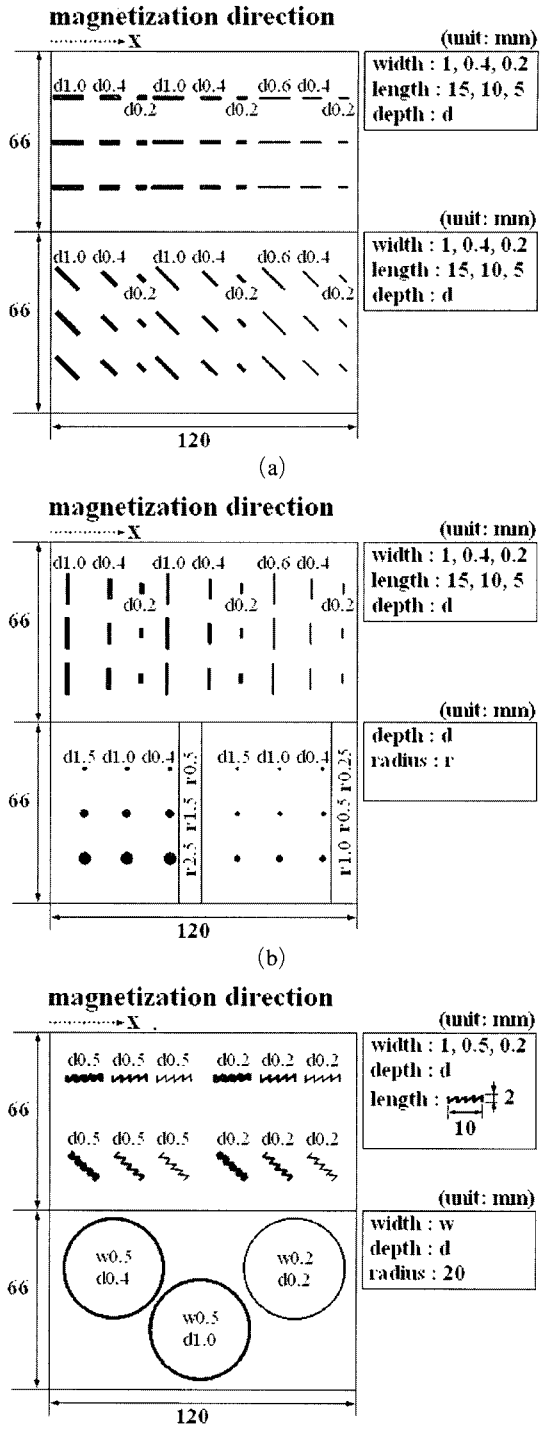

Fig. 6 Specimens

men by using electric discharge machining, as shown in Fig. 6. Their detailed shapes, sizes and relation with the magnetizing direction are shown in Table 1.

Table 1 Multiple cracks introduced on each specimen

Shape	Crack size [mm]			Volume [mm³] (cross section [mm²])
	length	depth	width	
rectangle type 0°, 45°, 90°	5	0.2	0.2	0.2 (0.04, 0.32, 1)
			0.4	0.4 (0.08, 0.32, 1)
			1.0	1.0 (0.20, 0.32, 1)
	10	0.4	0.2	0.8 (0.08, 0.89, 4)
			0.4	1.6 (0.16, 0.89, 4)
			1.0	4.0 (0.40, 0.89, 4)
	15	0.6	0.2	0.1 (0.12, 1.64, 9)
		1.0	0.4	6.0 (0.40, 2.74, 15)
			1.0	15.0 (1.00, 2.74, 15)
scratch type 0°, 45°	10	0.2	0.2	0.68 (0.4, 0.45)
			0.5	1.56 (0.4, 0.45)
			1.0	2.63 (0.4, 0.45)
		0.5	0.2	1.72 (1, 1.12)
			0.5	3.89 (1, 1.12)
			1.0	6.59 (1, 1.12)
Shape	Crack size [mm]			Volume [mm³] (cross section [mm²])
	radius	depth	width	
hole type	0.25	0.4		0.08 (0.2)
		1.0		0.19 (0.5)
		1.5		0.29 (0.75)
	0.5	0.4		0.31 (0.4)
		1.0		0.79 (1)
		1.5		1.17 (1.5)
	1	0.4		1.25 (0.8)
		1.0		3.14 (2)
		1.5		4.71 (3)
	1.5	0.4		2.83 (1.2)
		1.0		7.06 (3)
		1.5		10.60 (4.5)
	2.5	0.4		7.85 (2)
		1.0		19.63 (5)
		1.5		29.45 (7.5)
ring type	20	0.2	0.2	5.02 (8)
		0.4	0.5	25.13 (16)
		1.0		62.83 (48)

Figure 7(a) shows the analysis results of the Fig. 6(a) specimen, which were obtained by using the Eqs. (2) ~ (4) at the lift-off of 3 mm and $m/4\pi\mu=10$. The magnetic flux leakage from the magnetizer poles could be expressed as a large crack with a length of 180 mm, width of 150 mm and depth of 200 mm. According to the analysis results, the LMF distribution was significantly slanted due to the magnetizer poles, and the crack could not be visualized accurately due to weak LMF. Also, the experiment results showed slanted LMF distribution and little LMF around the crack as shown in Fig. 7(b). The crack could not be distinguished by using LMF distribution in both analysis and experiment.

However, the crack information was extracted by using the change in the LMF distribution according to the magnetization direction, $\partial B/\partial x$ image, as shown in Fig. 8, because of certain changes of LMF distribution around the crack. The figure shows the contour lines which divided the full range of 0 to 0.2 into 10 pieces at the $\partial B/\partial x$ distribution. On the other hand, the full range of the analysis result shows the sensor sensitivity. For example, when the full range is defined as 0.1 and 0.01 as shown in Figs. 9(a) and (b), the cracks that could not be visualized, as shown in Fig. 8(a), could be visualized. The full range was defined as 0.2 in this study, because the analysis results were similar with the experiment results at lift-off of 3 mm, as shown in Fig. 8.

On the other hand, the result of Fig. 8(b) showed strips in the X-axis direction. These strips developed because each sensor was not parallel to the printed circuit board surface. The analysis and experiment results based on the $\partial B/\partial x$ distribution, as shown in Figs. 8(a) and (b), showed the presence of cracks. However, no crack is confirmed on the top half of Fig. 8(b) because the magnetizing direction and the crack length direction were located on the same axis and the LMF was minimized. At the bottom half, the cracks having widths of 1.0 mm, lengths of 10 and 15 mm are present in the magnetizing direction at 45°,

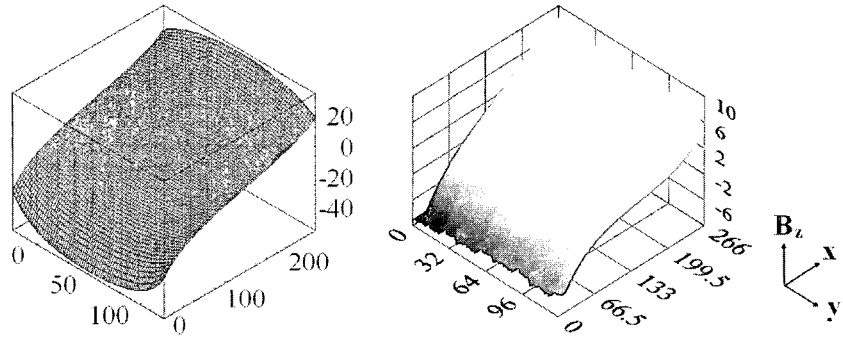

(a) Analysis result (b) Experiment result

Fig. 7 Analysis and experiment results of LMF distribution of Fig. 6(a) specimen

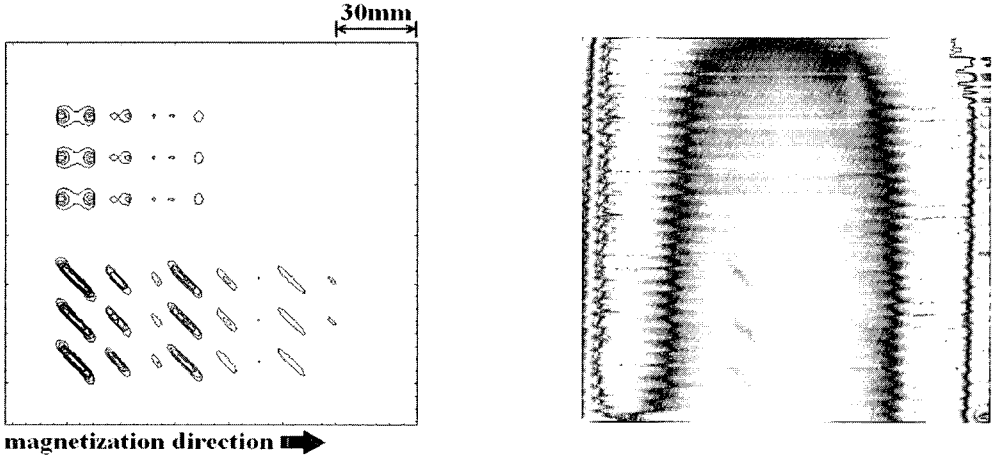

(a) Analysis result (b) Experiment result

Fig. 8 Analysis and experimental $\partial B/\partial x$ images of Fig. 6(a) specimen

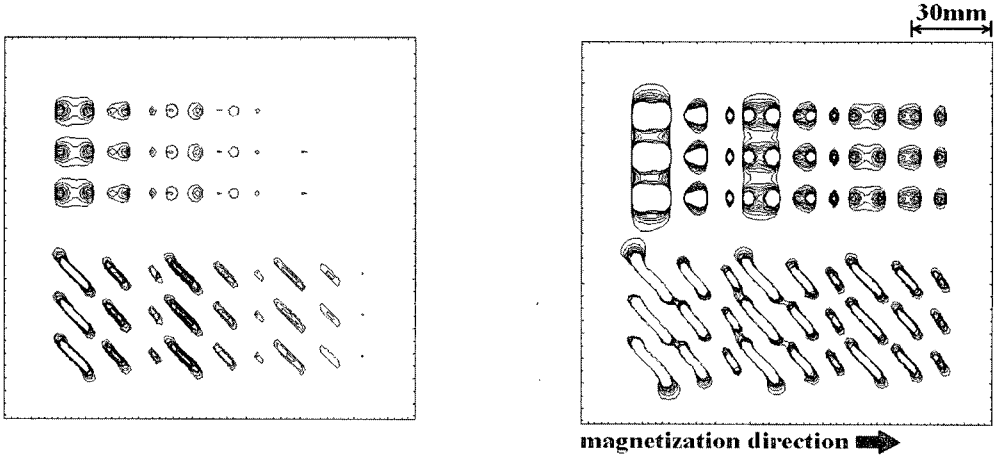

(a) Full range 0.1 (b) Full range 0.01

Fig. 9 Analyzed $\partial B/\partial x$ images according to full range

and other cracks with width of 0.4 mm and lengths of 10 and 15 mm are also present. When θ_C is 90°, as shown in the top half portion of Fig. 10 (b), cracks are shown distinctively, because the LMF was maximized. Cracks with a length of 15 mm and widths of 0.2, 0.4, and 1.0 mm and other cracks with a length of 10 mm and widths of 0.4 mm and 1.0 mm were visualized. At the bottom half portion of the figure, the hole type cracks with radius between 1.0 to 2.5 mm are detected, regardless of depth. And the cracks of the same shape with radius of 0.5 mm and depth of 1.0 mm were detected.

The θ_C of the scratch type cracks are 45° and 0°, as shown in the top half portion in Fig. 6(c). As shown in Fig. 11, the slanted cracks can be detected when the depth of crack is 0.5 mm and the widths are 0.2, 0.5 and 1.0 mm. Also, the cracks of a depth of 0.2 mm and widths of 0.5 and 1.0 mm were detected. However, cracks were not detected when θ_C was 0°. Also, only the ring type cracks with diameter of 40 mm, depths of 0.4 and 1.0 mm, and width of 0.5 mm are visualized in the bottom half portion of the figure.

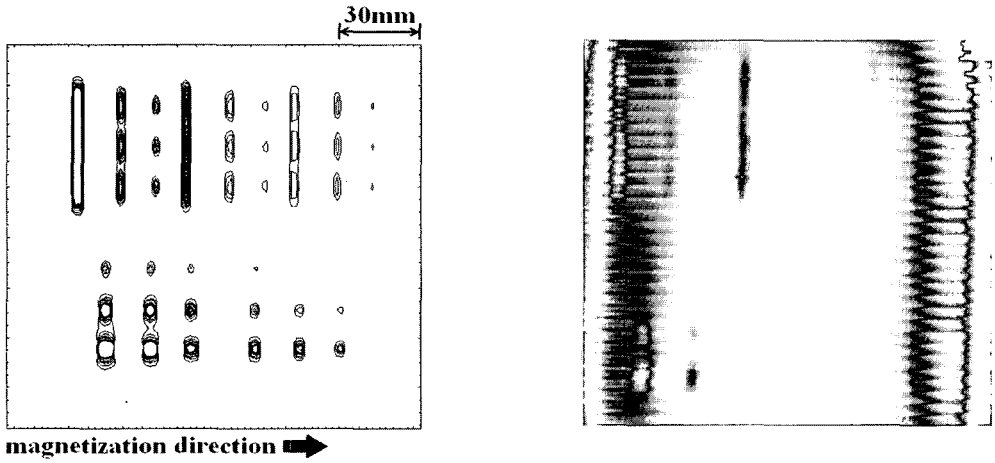

(a) Analysis result (b) Experiment result

Fig. 10 Analysis and experimental $\partial B/\partial x$ images of specimen shown in Fig. 6(b)

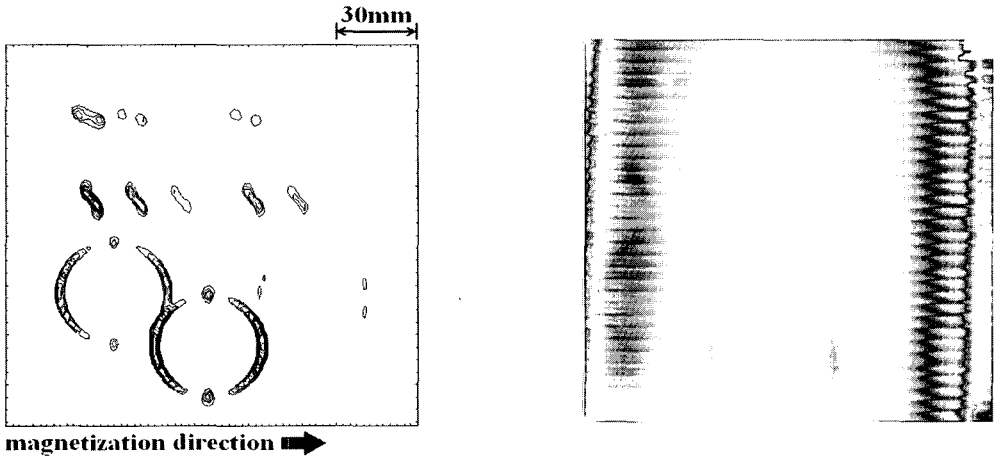

(a) Analysis result (b) Experiment result

Fig. 11 Analysis and experimental $\partial B/\partial x$ images of specimen of Fig. 6(c)

Conversely, as shown in Figs. 10~12, all of the experimental results could be simulated using the improved dipole model and Eqs. (2)~(6). Correspondingly, the improved dipole model can be used to simulate the LMF and $\partial B/\partial x$ image of a specimen with complex cracks, and to evaluate the cracks quantitatively using MFLT.

4. Discussion on the Quantitative Evaluation

Quantitative nondestructive evaluation measures and estimates the location, direction, length and volume of a crack. As mentioned above, LMF developed around the cracks of the magnetized specimens, and the LMF distribution sloped to the x-axis, the direction of magnetization, as shown in Fig. 12. The small LMF distribution around a crack can be extracted by using the $\partial B/\partial x$ images. Thus, the crack position could be determined.

Alternately, the crack direction can be estimated by using $\partial B/\partial x$ images, as shown in Fig. 8, Figs. 10 and 11 when the θ_C is not approximately 90°. Also, according to the recent research results (Lee and Hwang, 2006e), the crack can be detected without consideration of the crack direction by using a cross type magnetizer, which introduces a secondary magnetizer with in the direction vertical to the magnetizing direction of the previous yoke type magnetizer. Also, the crack direction can be estimated by using the $\partial B/\partial x$ image.

However, the $\partial B/\partial x$ image of the rectangle type crack with 45° θ_C, shown in the bottom half portion in Fig. 8, and the scratch type crack shown in the top half portion of Fig. 11 were difficult to distinguish. Also, the $\partial B/\partial x$ image of the rectangle type crack with a small crack length and 90° θ_C in the top half portion of Fig. 10 shows 3 distinguished cracks, but the $\partial B/\partial x$ images with a large crack length show that the 3 cracks were connected cracks. Considering that the structure, which had large cracks on the coincident axis, can be easily fractured, the illusion, which looks like a large crack on the $\partial B/\partial x$

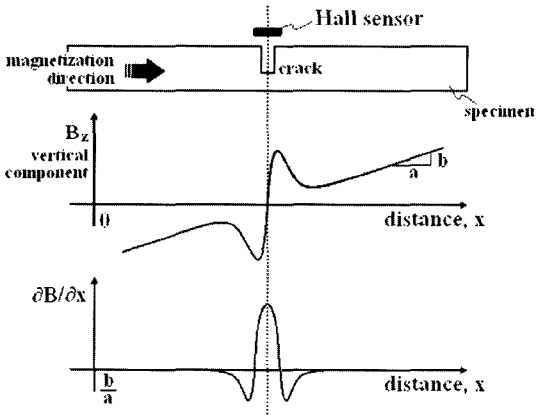

Fig. 12 Relationship between crack position and $\partial B/\partial x$ distribution

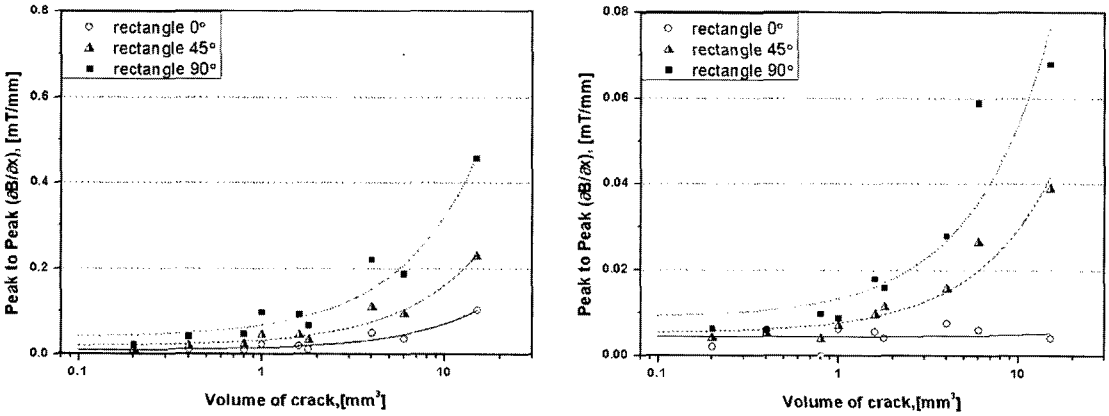

(a) Analysis result (b) Experiment result

Fig. 13 Relationship between crack volume and peak-to-peak of $\partial B/\partial x$

image, can provide useful information, i.e., an indication of a dangerous crack.

Conversely, the crack volume can be estimated when θ_C is known. The LMF and the maximum value of $\partial B/\partial x$ on the top of a crack were increased when the crack volume was increased. Also, the $\partial B/\partial x$ distribution was approximately homogeneous at the no crack area. Correspondingly, the difference between $\partial B/\partial x$ (hereafter, Max[$\partial B/\partial x$]) at the crack area and that at the no crack area is increased with the increase of the crack volume, as shown in Fig. 13.

The crack volume can be numerically estimated when θ_C is 0°, 45° and 90° in the rectangle type cracks with the Max[$\partial B/\partial x$], as shown in Fig. 13(a). Also, the experimental relationship between the crack volume and the Max[$\partial B/\partial x$] shows that the scan type magnetic camera images can be successfully estimated by using the dipole model, as shown in Fig. 13(b). However, the calculated Max[$\partial B/\partial x$] values did not coincide with the experimentally obtained Max[$\partial B/\partial x$] because the magnetic charge per unit area, m, and the magnetic permeability, μ, were set as contants in this paper.

5. Conclusions

The $\partial B/\partial x$ image, an image produced by the scan type magnetic camera, of multiple cracks of different shapes and sizes was calculated by using the improved dipole model in this paper. The improved dipole model was obtained by using small divided dipole models, the rotations and relocations of each dipole model, and the principle of superposition. The sensitivity of the magnetic sensors was expressed as $m/4\pi\mu$ and the full scale at the analyzed $\partial B/\partial x$ image. Also, for the low carbon steel specimen, the experimental results that considered the several sizes and shapes of the multiple cracks were compared with the modeling results to verify the effectiveness of the $\partial B/\partial x$ image modeling. The $\partial B/\partial x$ images using the improved dipole model allowed for qualitative evaluation of cracks with respect to the location, direction, length and volume of the crack.

Acknowledgements

This study was supported by research funds from Chosun University, 2006.

References

Lee, J. et al., 1998a, "Novel NDI by Use of Magneto-Optical Film," *Transactions of the Japan Society of Mechanical Engineers*, Vol. 64, No. 619, pp. 825~830.

Lee, J. et al., 1998b, "Nondestructive Inspection for the Paramagnetic Materials Using the Magneto-Optical NDI System," *Journal of the Japan Society of Applied Electromagnetics and Mechanics*, Vol. 6, No. 4, pp. 337~342.

Lee, J. et al., 2000, "An Algorithm for the Characterization of Surface Crack by Use of Dipole Model and Magneto-Optical Non-Destructive Inspection System," *KSME International Journal*, Vol. 14, No. 10, pp. 1072~1080.

Lee, J. et al., 2001, "Development of Magnetic Camera Using 2-D Arrayed Hall Elements," Proc. APCFS & ATEM'01, pp. 222~227.

Lee, J. et al., 2004a, "Magnetic Flux Density Apparatus for, E.G., Detecting an Internal Crack of a Metal or a Shape of the Metal," US patents 6,683,452 B2.

Lee, J. et al., 2004b, "Theoretical Consideration of Nondestructive Testing by Use of Vertical Magnetization and Magneto-Optical Sensor," *KSME International Journal*, Vol. 18, No. 4, pp. 640~648.

Lee, J. et al., 2004c, "Numerical Consideration of Magnetic Camera for Quantitative Nondestructive Evaluation," *Key Engineering Materials*, Vols. 270~273, pp. 630~635.

Lee, J. et al., 2005, "Modeling of Characteristics of Magneto-Optical Sensor Using FEM and Dipole Model for Nondestructive Evaluation," *Key Engineering Materials*, Vols. 297~300, pp. 2022~2027.

Lee, J. et al., 2006a, "The QNDE Using Image Processing of the Magnetic Camera," *International Journal of Modern Physics B*, in press.

Lee, J. et al., 2006b, "Detection Probability

Improvement for Nondestructive Evaluation Using a Magnetic Camera," *Key Engineering Materials*, Vols. 306~308, pp. 241~246.

Lee, J. et al., 2006c, "A Study of Leakage Magnetic Flux Detector Using Hall Sensors Array," *Key Engineering Materials*, Vols. 306~308, pp. 235~240

Lee, J. et al., 2006d, "The Detection Probability Improvement of the Far-Side Crack on the High Lift-off Using the Magnetic Camera," *International Journal of Modern Physics B*, in press.

Lee, J. and Hwang, J., 2006e, "A Study of the Quantitative Nondestructive Evaluation Using the Cross Type Magnetic Source and the Magnetic Camera," *Key Engineering Materials*, Vol. 321-323, pp. 1447~1450.

Minkov, D. et al., 2000, "Improvement of the Dipole Model of a Surface Crack," *Materials Evaluation*, Vol. 58, No. 5, pp. 661~666.

Mukae, S., 1988, "Investigation of Quantification for Defect and Effect of Factors Affecting Leakage Flux Density in Magnetic Leakage Flux Testing Method," *Journal of the Japanese Society for Non-Destructive Inspection*, Vol. 37, No. 11, pp. 885~894.

Yamada, K. et al., 2001, "Magnetic and Optical Nondestructive Evaluations for Iron-based Materials," *Nondestructive Characterization of Materials X*, Elsevier, pp. 330~340.